Novel Fitting Algorithm for Parametrization of Equivalent Circuit Model of Li-Ion Battery From Broadband Impedance Measurements

Jussi Sihvo, *Student Member, IEEE*, Tomi Roinila, *Member, IEEE*, and Daniel-Ioan Stroe, *Member, IEEE*

***Abstract*—The impedance of lithium-ion (Li-ion) batteries contains information about the dynamics and state parameters of the battery. This information can be utilized to improve the performance and safety of the battery application. The battery impedance is typically modeled by an equivalent-circuit-model (ECM), which provides the dynamic information of the battery. In addition, the variations in the model parameters can be used for the battery state estimation. A fitting algorithm is required to parametrize the ECM due to the nonlinearity of both the battery impedance and ECM. However, conventional fitting algorithms, such as the complex-nonlinear-least-squares (CNLS) algorithm, often have a high computational burden and require selection of initial conditions, which can be difficult to obtain adaptively. This article proposes a novel fitting algorithm for the parametrization of battery ECM based on the geometric shape of the battery impedance in the complex-plane. The algorithm is applied to practical and fast broadband pseudorandom sequence impedance measurements carried out at various state-of-charges (SOC) and temperatures for lithium-iron-phosphate cell. The performance of the method is compared to conventional CNLS algorithm with different initial conditions. The results show that the proposed method provides fast and accurate fit with low computational effort. Moreover, specific ECM parameters are found to be dependent on the battery SOC at various temperatures.**

Nomenclature

CNLS	Complex nonlinear least squares.
ECM	Equivalent circuit model.
EIS	Electrochemical impedance spectroscopy.
EoD	End of the diffusion.
LiFePO4	Lithium iron phosphate.
PRS	Pseudo random sequence.
NRMSE	Normalized root mean square error.
SEI	Solid electrolyte interface.
SOC	State of charge.
SOH	State of health.
TSC	Top of the semicircle.
f_{gen}	Generation frequency of PRS.
f_{res}	Frequency resolution of PRS measurements.
C_{CT}	Capacitance of the charge-transfer region.
C_{D}	Capacitance of the diffusion region.
N	Length of the PRS period.
α_{CT}	Suppression factor of charge-transfer region.
α_{D}	Suppression factor of diffusion region.
k	Iteration index.
L_{s}	Series inductance.
R_{CT}	Resistance of the charge-transfer region.
R_{EoD}	Real-part of the end of the diffusion.
R_{minreal}	Minimum real-part of the impedance.
R_{TSC}	Real-part of the top of the semicircle.
R_{s}	Series resistance.
X_{EoD}	Imaginary-part of the end of the diffusion.
X_{minreal}	Imaginary-part of the minimum real-part.
X_{TSC}	Imaginary-part of the top of the semicircle.
Z_{ECM}	Equivalent circuit model impedance.
Z_{CT}	Charge-transfer region impedance.
$Z_{\text{CT-im}}$	Imaginary-part of the charge-transfer region.
$Z_{\text{CT-re}}$	Real-part of the charge-transfer region.
Z_{D}	Diffusion region impedance.
Z_{fit}	Model-fitted impedance.
Z_{meas}	Measured impedance.

Manuscript received October 30, 2019; revised January 31, 2020, February 28, 2020, and March 27, 2020; accepted April 5, 2020. Date of publication April 27, 2020; date of current version February 17, 2021. This was supported by the Tiina ja Antti Herlin Foundation in Finland. *(Corresponding author: Jussi Sihvo.)*

Jussi Sihvo and Tomi Roinila are with the Faculty of Information Technology, Tampere University 33100, Tampere, Finland (e-mail: jussi.sihvo@tuni.fi; tomi.roinila@tuni.fi).

Daniel-Ioan Stroe is with the Department of Energy Technology, Aalborg University 9100, Aalborg, Denmark (e-mail: dis@et.aau.dk).

Color versions of one or more of the figures in this article are available online at https://ieeexplore.ieee.org.

Digital Object Identifier 10.1109/TIE.2020.2988235

I. Introduction

THE increasing usage of lithium-ion (Li-ion) batteries in electrical transportation and renewable energy storage applications is introducing strict demands for the safety and performance monitoring of Li-ion batteries. The monitoring of Li-ion batteries is based on the estimation of the battery state parameters, such as, state-of-charge (SOC) and state-of-health (SOH), which are indirectly obtained from the voltage, current, and temperature measurements of the battery system. Conventional estimation methods are based on the voltage-profile and coulomb-counting methods for the SOC estimation, and capacity-fade and internal dc resistance methods for the SOH estimation [1], [2]. However, as the power and energy levels

of the battery systems increase, more state-estimation methods along with the existing ones are required to guarantee the performance of such applications in the future.

It is widely recognized that the ac impedance of a Li-ion battery is highly dependent on the battery state parameters [1]–[4]. To investigate both the battery dynamics and the variations in the impedance for the SOC and SOH estimation, the impedance is usually mapped to nonlinear equivalent-circuit-model (ECM) parameters [3], [5]–[8]. Due to the nonlinearity of the ECM, an optimization algorithm, such as particle-swarm-optimization [7] or complex-nonlinear-least-squares (CNLS) algorithm, is required to fit the ECM accurately to the impedance data [3], [9]. Although these algorithms are effective, they have high computational requirements and require initial conditions for the ECM parameters. Moreover, the selection of the initial values affects on the performance of the algorithm that should be as close to the eventual fit as possible [10]. Recent studies have proposed initialization methods for the parameters [11]–[15]. However, some parameters have been found difficult to initialize adaptively based on the impedance data. This is the case with the fractional-order element, also known as the suppression factor. Moreover, the simplifications made to the derivation of other ECM parameters (e.g., capacitances and inductances) are insufficient because of the nonlinearity, and the strong cross correlation of high-frequency terms of the ECM. However, adaptively obtained accurate initial conditions can not only improve the performance of the fitting algorithm in changing operating conditions of the battery, but can also reduce the complexity needed for the fitting algorithm [15]. This presents an opportunity to design the algorithm in a lighter manner than the conventional algorithms, making it more suitable for practical applications.

In order to utilize impedance information for the battery system, it is necessary to measure the impedance onboard in the battery system. The traditional method for the impedance measurements is the electrochemical impedance spectroscopy (EIS) [16]–[19]. While this method provides accurate results, the long measurement time and high complexity of the sinusoid generation require to simplify its implementation for onboard battery applications [19], [20]. To keep the measurements' complexity low, step and pulse excitations, such as hybrid-pulse-power-characterization (HPPC) test, can be applied [3], [7]. The method is an effective way to obtain the SOC, SOH, current, and temperature dependency of the impedance but it requires several pulses to be injected, which prolongs the measurements. To achieve fast measurements, broadband signals, such as, multisines [16] and pseudo-random-sequences (PRS) can be used [21]–[23]. PRS signals are especially attractive because they can be designed with a finite number of signal levels, which significantly reduces the complexity of the method implementation. However, most of the PRS signals are only suitable for measuring linear systems that restricts their use for battery applications, which are nonlinear [21], [22]. Nevertheless, recent studies have reported that a three-level PRS (regarded as a ternary sequence) has good performance under system nonlinear effects in battery applications [15], [24]. Because of the reduced measurement time, low complexity, and good performance under system nonlinearities, the ternary sequence is wellsuited for practical battery impedance measurements.

This article proposes a novel fitting algorithm for battery impedance ECM parametrization. The algorithm consists of two parts: the initialization and optimization processes. In both processes, the geometric shape of the impedance plot is utilized for the parametrization. The performance of the algorithm is validated to lithium-iron-phosphate (LiFePO4) cell impedance, measured by a broadband ternary sequence excitation signal applied at various SOCs and temperatures. The algorithm is shown to produce accurate fit and to have more consistent performance at all SOCs and temperatures than the CNLS. The required low computational effort also makes the algorithm very fast compared to conventional CNLS algorithm. Moreover, the proposed initialization can adaptively provide the initial conditions for the CNLS which can yield to more robust performance in changing operating conditions. In addition, some of the fitted ECM parameters are shown to have clear dependency to the battery SOC and temperature. Thus, along with the ternary-sequence measurements, the proposed algorithm has the potential to be utilized for battery dynamic analysis and state estimation in practical battery applications.

The rest of this article is organized as follows. The applied impedance ECM model is presented in Section II and the proposed fitting algorithm is introduced in Section III. The impedance measurements and the design of the ternary-sequence excitation signal are presented in Section IV. The experiments and the obtained results are discussed and presented in Sections V and VI, respectively. Section VII concludes this article.

II. Impedance Model

A typical impedance plot of a LiFePO4 cell along with the used ECM is shown in Fig. 1. The imaginary-axis in Fig. 1 is inverted to illustrate the plot in the first quadrant in the complex plane. In the impedance plot, three main regions can be identified, each caused by different electrochemical processes in a battery cell. The diffusion region in the low frequencies ($<$3 Hz) represents the solid-state diffusion of lithium-ions within the bulk of the electrode material. The charge-transfer region is realized by the charge-transfer and electrochemical double-layer reactions at frequencies between 3 Hz and 1 kHz. The ohmic/inductive region represents the effect of current collectors and wires, usually realized at high frequencies ($>$1 kHz). Depending on the battery chemistry, temperature, SOH, and SOC, the impedance can also include other distinctive regions. Along with the charge-transfer region semicircle, a second semicircle may appear at very low temperatures and low SOH caused by the formation of a solid-electrolyte-interface (SEI) layer. However, the SEI effect for the impedance of the LiFePO4 cell can be considered negligible, which is why it is not visible in the impedance spectrum presented in Fig. 1. [11], [19], [25]

A typical ECM for the LiFePO4 cell impedance is shown at the bottom of Fig. 1, where the nonlinearities of the impedance are modeled by a constant-phase-element (CPE) as

$$Z_{\text{CPE}} = \frac{1}{(j\omega)^{\alpha} C}. \tag{1}$$

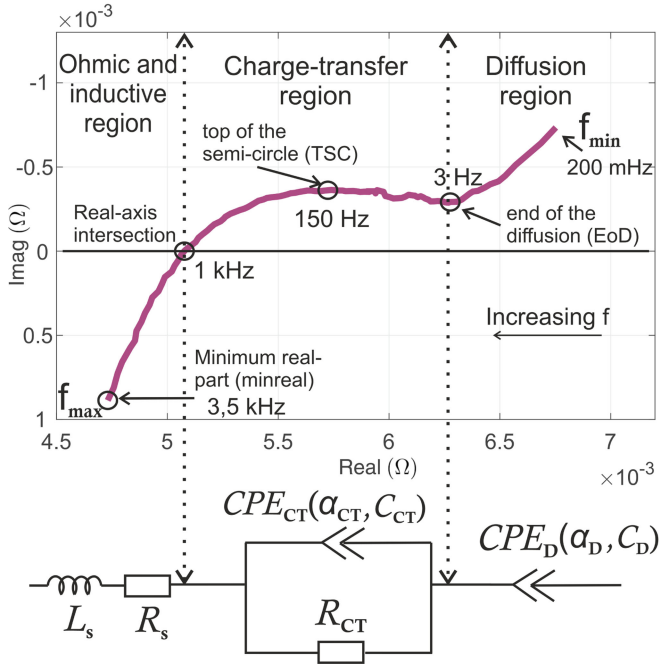

Fig. 1. Measured impedance plot of a LiFePO4 battery cell along with the corresponding ECM.

In (1), C is the capacitance and α is the suppression factor having values between 0 (pure resistance) and 1 (pure capacitance) [6]–[8], [11]–[13]. The ECM in Fig. 1 can be expressed as

$$Z_{\text{ECM}} = j\omega L_{\text{s}} + R_{\text{s}} + Z_{\text{CT}} + Z_{\text{D}} \tag{2}$$

where L_{s} is the inductance of the series inductor and R_{s} is the series resistance that together models the ohmic/inductive region of the impedance. Z_{CT} given in (3) represents the charge-transfer region impedance. The suppressed semicircle shape is obtained with the parallel connection of a resistor and CPE. For the further parametrization of the model, it is convenient to separate real and imaginary parts of Z_{CT}, which are given in (4) and (5), respectively. Z_{D} represents the diffusion region impedance in which the constant-slope behavior can be modeled by using a single CPE. The diffusion region impedance is given in both complex and separated real and imaginary parts forms in (6). For the resistors, capacitors, and suppression factors in (3)–(6), the subscripts "CT" and "D" denote the charge-transfer region and diffusion region parameters, respectively.

$$Z_{\text{CT}} = \frac{1}{\frac{1}{R_{\text{CT}}} + (j\omega)^{\alpha_{\text{CT}}} C_{\text{CT}}} \tag{3}$$

$$Z_{\text{CT-re}} = \frac{R_{\text{CT}} + \cos(\frac{\pi\alpha_{\text{CT}}}{2}) R_{\text{CT}}^2 C_{\text{CT}} \omega^{\alpha_{\text{CT}}}}{1 + 2\cos(\frac{\pi\alpha_{\text{CT}}}{2}) R_{\text{CT}} C_{\text{CT}} \omega^{\alpha_{\text{CT}}} + \omega^{2\alpha_{\text{CT}}} R_{\text{CT}}^2 C_{\text{CT}}^2} \tag{4}$$

$$Z_{\text{CT-im}} = \frac{-j\sin(\frac{\pi\alpha_{\text{CT}}}{2}) R_{\text{CT}}^2 C_{\text{CT}} \omega^{\alpha_{\text{CT}}}}{1 + 2\cos(\frac{\pi\alpha_{\text{CT}}}{2}) R_{\text{CT}} C_{\text{CT}} \omega^{\alpha_{\text{CT}}} + \omega^{2\alpha_{\text{CT}}} R_{\text{CT}}^2 C_{\text{CT}}^2} \tag{5}$$

$$Z_{\text{D}} = \frac{1}{(j\omega)^{\alpha_{\text{D}}} C_{\text{D}}} \Longleftrightarrow \frac{\cos(\frac{\pi\alpha_{\text{D}}}{2})}{\omega^{\alpha_{\text{D}}} C_{\text{D}}} - \frac{j\sin(\frac{\pi\alpha_{\text{D}}}{2})}{\omega^{\alpha_{\text{D}}} C_{\text{D}}}. \tag{6}$$

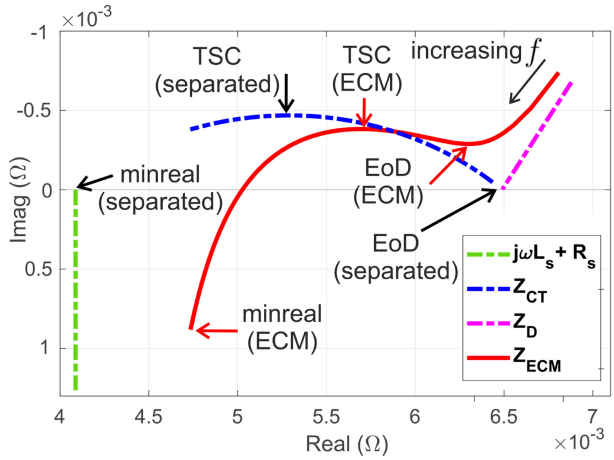

Fig. 2. Discrepancy illustration of the individual parts of ECM with respect to the total ECM in the frequency range of 200 mHz–3.5 kHz.

The impedance plot in Fig. 1 also contains points that are important for the parametrization of the ECM. These points are the zero-derivative points and the minimum real-part. The first zero-derivative point is realized at the intersection of the diffusion and charge-transfer regions and is regarded as the end-of-the-diffusion (EoD). The second zero-derivative point is realized at the top-of-the-semicircle (TSC) at the charge-transfer region. The minimum real-part is simply the lowest real-part occurring in the impedance. It is also worth mentioning the boundary between the charge-transfer and ohmic/inductive regions, which is typically considered at the point where the battery impedance intersects the real axis. The point is often used to model the battery aging and the SOH [5], [17]. However, same information can be obtained from the minimum real part which is why the real-axis intersection point is not further used in this article.

III. Proposed Fitting Algorithm

The proposed fitting algorithm consists of two parts, the initialization and iteration processes. The initialization process aims to produce satisfying fit that provides a good start point for the iterative process to converge quickly. The initialization process alone is insufficient to obtain accurate fit due to the nonlinearity of the ECM and strong cross correlation of the impedance regions in the model. This is illustrated in Fig. 2, where fitted Z_{ECM} and its separately plotted terms ($j\omega L_{\text{s}} + R_{\text{s}}$, Z_{CT} and Z_{D}) have huge discrepancies. Thus, the zero-derivatives at the EoD and TSC, along with the minimum real-part, are also found in a slightly different locations in the complex plane. This introduces error to the initialization process, since the zero-derivatives are obtained from the measurements while the separated terms are mostly used for the parameter calculations. Therefore, an iterative process is required in order to guarantee the performance of the algorithm. The algorithm is applied to impedance data provided from the battery impedance measurements, which are discussed later in Section IV. In further parts of this section, the parameters in (2)–(6) are included with a superscript indicating the iteration index k.

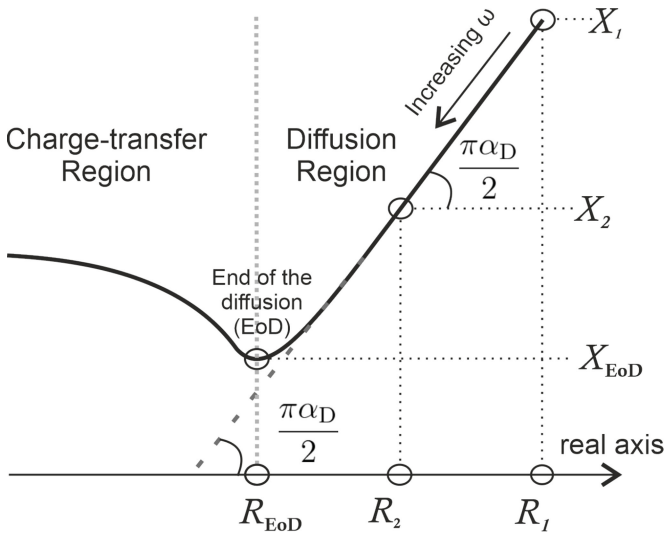

Fig. 3. Parameter and subparameter illustration of the ECM in the diffusion region.

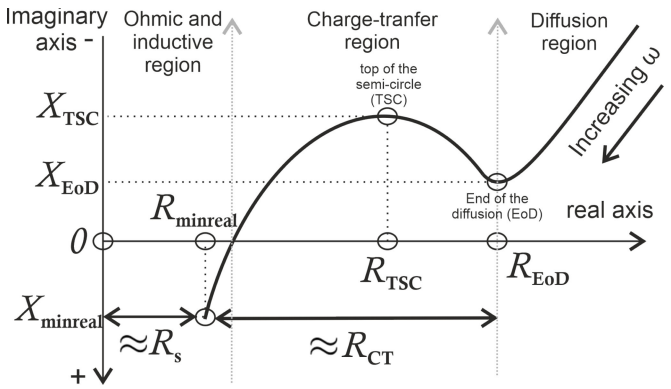

Fig. 4. Parameter and subparameter illustration of the ECM in the charge-transfer and ohmic/inductive regions.

A. Initialization

The initialization process starts with the extraction of the zero-derivative points at the EoD (R^0_{EoD}, X^0_{EoD}) and at the TSC (R^0_{TSC}, X^0_{TSC}), along with the minimum real-part ($R^0_{minreal}$, $X^0_{minreal}$) from the impedance data. In addition, two arbitrary data points at the diffusion region, (R^0_1, X^0_1) and (R^0_2, X^0_2) are required. The superscript denotes the iteration index $k = 0$ at the initialization process. The locations of these subparameters are illustrated in Figs. 3 and 4 (without the iteration index). These sub-parameters can be extracted numerically from the complex impedance data and they are also needed in the iteration process and must be stored throughout the fitting algorithm.

At the diffusion region, the initial value of the suppression factor α^0_D can be obtained from the angle between the impedance slope and the real axis as illustrated in Fig. 3 [15]. Thus, α^0_D can be derived as

$$\alpha^0_D = \frac{2}{\pi}\text{atan}\left(\frac{X^0_1 - X^0_2}{R^0_1 - R^0_2}\right) \tag{7}$$

where R^0_1 and R^0_2 are the real parts, and X^0_1 and X^0_2 are the imaginary parts of the two arbitrary data points in the diffusion region. By using either of these data points, C^0_D can be calculated from the imaginary part in (6) as

$$C^0_D = -\frac{\sin\left(\frac{\pi\alpha^0_D}{2}\right)}{\omega_1^{\alpha^0_D} X^0_1}. \tag{8}$$

At the ohmic/inductive and charge-transfer regions, the initial value of the series resistance R^0_s can be approximated as the minimum real part of the impedance given in (9). The initial value of the resistance R^0_{CT} is given by the width of the semicircle (as shown in Fig. 4) given in (10) [13], [15]

$$R^0_s \approx R^0_{minreal} \tag{9}$$

$$R^0_{CT} \approx R^0_{EoD} - R^0_{minreal}. \tag{10}$$

For the initialization of α^0_{CT}, its correlation to the imaginary-part at TSC can be utilized. For simplicity, the model is reduced at this point to consist only of the charge-transfer region impedance imaginary part in (5). Moreover, the iteration index notations are neglected from the superscript for simplicity. When obtaining the zero derivative of (5) in terms of $\omega^{\alpha_{CT}}$ to obtain the angular frequency at the TSC, we get

$$\frac{dZ_{CT\text{-}im}}{d\omega^{\alpha_{CT}}} = 0 \Longleftrightarrow \omega^{\alpha_{CT}}_{TSC} = \frac{1}{R_{CT}C_{CT}}. \tag{11}$$

When substituting the resulting (11) back to (5) and reorganizing the terms, the following relation can be obtained

$$Z_{CT\text{-}im}(\omega^{\alpha_{CT}}_{TSC}) = X_{TSC} = \frac{R_{CT}\sin\left(\frac{\pi\alpha_{CT}}{2}\right)}{2\left(\cos\left(\frac{\pi\alpha_{CT}}{2}\right)+1\right)}. \tag{12}$$

Equation (12) shows that X_{TSC} is independent of the capacitor value and is defined only by α_{CT} and R_{CT}. Therefore, α_{CT} can be solved from (12) as in (13), where the iteration index is again presented

$$\alpha^0_{CT} = \frac{4}{\pi}\text{atan}\left(\frac{X^0_{TSC}}{\frac{R^0_{CT}}{2}}\right). \tag{13}$$

The impedance at the TSC can also be used for the extraction of C^0_{CT}. $Z^0_{CT\text{-}re}$ in (4) can be arranged in terms of C^0_{CT} as in (14), from which the solution for C^0_{CT} is given by the quadratic equation. Deriving C^0_{CT} from the real-part instead of the imaginary part is useful because series inductance is not required for the calculations

$$\begin{aligned} &a_C {C^0_{CT}}^2 + b_C C^0_{CT} + c_C = 0 \\ &a_C = R^0_{TSC}{R^0_{CT}}^2\omega^{2\alpha^0_{CT}}_{TSC} \\ &b_C = \cos\left(\frac{\pi\alpha^0_{CT}}{2}\right)R^0_{CT}\omega^{\alpha^0_{CT}}_{TSC}\left(2R^0_{TSC} - R^0_{CT}\right) \\ &c_C = R^0_{TSC} - R^0_{CT}. \end{aligned} \tag{14}$$

For the initialization of L^0_s, charge-transfer region impedance should be taken into account due to the strong cross correlation of the ohmic/inductive and charge-transfer regions. Because the

inductive behavior of the impedance is higher toward higher frequencies, a data point in the ohmic/inductive region should be used for the calculations. The imaginary part of the minimum real-part of the impedance curve can be used for this purpose, since the point is already extracted for (9). By incorporating the $Z^0_{\text{CT-im}}$ in (5) with the conventional inductor impedance equation ($j\omega L^0_s$) and solving L^0_s, we get the following equation for the series inductance:

$$L^0_s = \frac{jX^0_{\text{minreal}} - Z^0_{\text{CT-im}}(\omega_{\text{minreal}})}{j\omega_{\text{minreal}}}. \tag{15}$$

The resulting fit from the initialization in (7)–(15) is not likely to accurately match the measurement data due to the simplifications made to the model during the initialization. However, the resulting impedance fit provides a good start point for the iteration process or more advanced fitting algorithms such as the CNLS.

B. Iteration

At the iteration process, the parameters from the previous iteration index $k-1$ are substituted to (2) and new subparameter values for $X^{\text{k}}_{\text{TSC}}$, R^{k}_1, X^{k}_1, R^{k}_2, and X^{k}_2 are extracted from the impedance model data. With all the parameters available from the previous iteration $k-1$, the value of R^{k}_s can be derived by using the real part in (2). At the ohmic/inductive region, the influence of diffusion region impedance is negligible and it can be neglected from the derivation. Therefore, R^{k}_s can be derived as given in (16).

$$R^{\text{k}}_s = R^0_{\text{minreal}} - Z^{\text{k-1}}_{\text{CT-re}}(\omega_{\text{minreal}}). \tag{16}$$

Similarly to R^{k}_s, the estimation accuracy of R^{k}_{CT} can now be improved by solving it directly from (2). The imaginary-part of (2) at the EoD is here used for the calculations but also the real part could be used. At the EoD, the effect of the series inductance can be considered negligible. Thus, (2) can be reduced to (17), which can be written open and arranged in terms of R^{k}_{CT} as in (18) with the coefficients a_{R}, b_{R}, and c_{R} given in (19) shown at the bottom of this page. The coefficients can be applied to the quadratic equation to obtain a solution for R^{k}_{CT}.

$$X^0_{\text{EoD}} = -\frac{j\sin\left(\frac{\pi\alpha^{\text{k-1}}_{\text{D}}}{2}\right)}{\omega^{\alpha^{\text{k-1}}_{\text{D}}}_{\text{EoD}} C^{\text{k-1}}_{\text{D}}} + Z^{\text{k-1}}_{\text{CT-im}}(\omega_{\text{EoD}}) \tag{17}$$

$$a_{\text{R}} {R^{\text{k}}_{\text{CT}}}^2 + b_{\text{R}} R^{\text{k}}_{\text{CT}} + c_{\text{R}} = 0 \tag{18}$$

$\alpha^{\text{k}}_{\text{CT}}$ can be readjusted by compensating the difference of the imaginary-part at the TSC between the original measurements (X^0_{TSC}) and the model derived at the current iteration ($X^{\text{k}}_{\text{TSC}}$) as given in (20). The absolute value of the difference $X^{\text{k}}_{\text{TSC}} - X^0_{\text{TSC}}$ in (20) is used as the convergence criteria for the algorithm. The value for C^{k}_{CT} is updated based on (14) already used in the initialization process by updating the coefficients as given in (21). The quadratic equation is then applied to solve C^{k}_{CT}. The value for L^{k}_s is obtained based on (15), where parameters are updated to correspond the current iteration given in (22).

For the diffusion region parameters, $\alpha^{\text{k}}_{\text{D}}$ is compensated according to the difference of the slopes between the measurements and the model derived at current iteration as given in (23). Finally, C^{k}_{D} is adjusted based on (7), where parameters are updated as given in (24). The presented algorithm is step-wisely summarized in Fig. 5.

$$\alpha^{\text{k}}_{\text{CT}} = \alpha^{\text{k-1}}_{\text{CT}} - \frac{4}{\pi}\text{atan}\left(\frac{X^{\text{k}}_{\text{TSC}} - X^0_{\text{TSC}}}{\frac{R^{\text{k}}_{\text{CT}}}{2}}\right) \tag{20}$$

$$a_{\text{C}} {C^{\text{k}}_{\text{CT}}}^2 + b_{\text{C}} C^{\text{k}}_{\text{CT}} + c_{\text{C}} = 0$$

$$a_{\text{C}} = R^0_{\text{TSC}} {R^{\text{k}}_{\text{CT}}}^2 \omega^{2\alpha^{\text{k}}_{\text{CT}}}_{\text{TSC}}$$

$$b_{\text{C}} = \cos\left(\frac{\pi\alpha^{\text{k}}_{\text{CT}}}{2}\right) R^{\text{k}}_{\text{CT}} \omega^{\alpha^{\text{k}}_{\text{CT}}}_{\text{TSC}} \left(2R^0_{\text{TSC}} - R^{\text{k}}_{\text{CT}}\right)$$

$$c_{\text{C}} = R^0_{\text{TSC}} - R^{\text{k}}_{\text{CT}} \tag{21}$$

$$L^{\text{k}}_s = \frac{jX^0_{\text{minreal}} - Z^{\text{k}}_{\text{CT-im}}(\omega_{\text{minreal}})}{j\omega_{\text{minreal}}} \tag{22}$$

$$\alpha^{\text{k}}_{\text{D}} = \alpha^{\text{k-1}}_{\text{D}} - \frac{2}{\pi}\left(\text{atan}\left(\frac{X^{\text{k}}_1 - X^{\text{k}}_2}{R^{\text{k}}_1 - R^{\text{k}}_2}\right) - \text{atan}\left(\frac{X^0_1 - X^0_2}{R^0_1 - R^0_2}\right)\right) \tag{23}$$

$$C^{\text{k}}_{\text{D}} = -\frac{\sin\left(\frac{\pi\alpha^{\text{k}}_{\text{D}}}{2}\right)}{\omega^{\alpha^{\text{k}}_{\text{D}}}_1 X^0_1}. \tag{24}$$

IV. Impedance Measurements

The impedance of a battery can be measured by exciting the battery with a current perturbation and measuring the voltage response. The measured current and voltage can then be Fourier-transformed to obtain the frequency response of the measurements. The impedance can then be obtained according to Ohm's law in the frequency domain as

$$Z(j\omega) = \frac{V(j\omega)}{I(j\omega)}. \tag{25}$$

The form of the excited pulse is very important because its frequency content determines the reliability of the measurement results. In the conventional EIS method, the sinusoidal excitation

$$a_{\text{R}} = X^0_{\text{EoD}} \omega^{2\alpha^{\text{k-1}}_{\text{CT}} + \alpha^{\text{k-1}}_{\text{D}}}_{\text{EoD}} {C^{\text{k-1}}_{\text{CT}}}^2 C^{\text{k-1}}_{\text{D}} + \sin\left(\frac{\pi\alpha^{\text{k-1}}_{\text{D}}}{2}\right) \omega^{2\alpha^{\text{k-1}}_{\text{CT}}}_{\text{EoD}} {C^{\text{k-1}}_{\text{CT}}}^2 + \sin\left(\frac{\pi\alpha^{\text{k-1}}_{\text{CT}}}{2}\right) \omega^{\alpha^{\text{k-1}}_{\text{CT}} + \alpha^{\text{k-1}}_{\text{D}}}_{\text{EoD}} C^{\text{k-1}}_{\text{CT}} C^{\text{k-1}}_{\text{D}}$$

$$b_{\text{R}} = 2\sin\left(\frac{\pi\alpha^{\text{k-1}}_{\text{D}}}{2}\right) \cos\left(\frac{\pi\alpha^{\text{k-1}}_{\text{CT}}}{2}\right) \omega^{\alpha^{\text{k-1}}_{\text{CT}}}_{\text{EoD}} C^{\text{k-1}}_{\text{CT}} + 2X^0_{\text{EoD}} \cos\left(\frac{\pi\alpha^{\text{k-1}}_{\text{CT}}}{2}\right) \omega^{\alpha^{\text{k-1}}_{\text{CT}} + \alpha^{\text{k-1}}_{\text{D}}}_{\text{EoD}} C^{\text{k-1}}_{\text{CT}} C^{\text{k-1}}_{\text{D}}$$

$$c_{\text{R}} = X^0_{\text{EoD}} C^{\text{k-1}}_{\text{D}} \omega^{\alpha^{\text{k-1}}_{\text{D}}}_{\text{EoD}} + \sin\left(\frac{\pi\alpha^{\text{k-1}}_{\text{D}}}{2}\right) \tag{19}$$

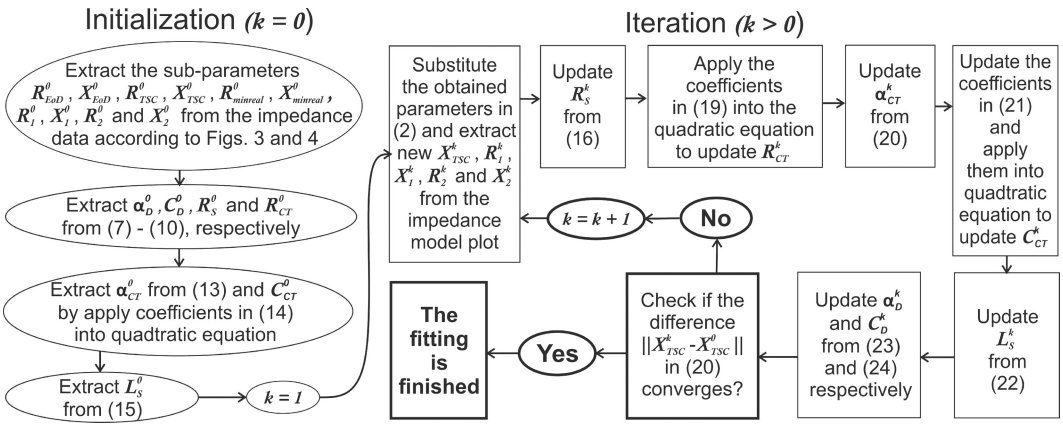

Fig. 5. Step-by-step block diagram of the proposed fitting algorithm.

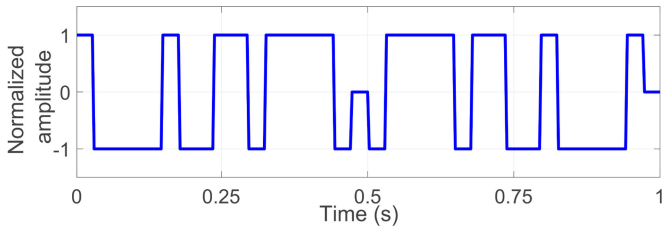

Fig. 6. Ternary-sequence in time domain ($f_{\text{gen}} = 34$ Hz and $N = 34$).

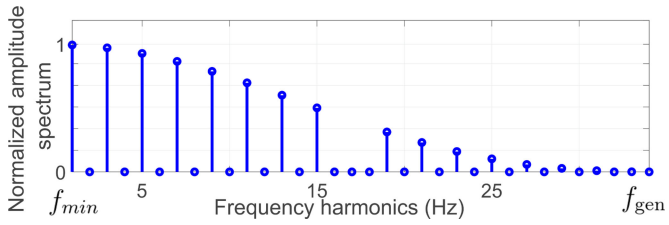

Fig. 7. Ternary-sequence in frequency domain ($f_{\text{gen}} = 34$ Hz and $N = 34$).

is utilized due to its good signal-to-noise ratio [16]. However, in theory, the sinusoidal excitation requires infinite number of signal levels, which complicates the implementation of the method to an application. Moreover, it is also very slow method because the sinusoid contains energy only at the fundamental frequency and every frequency harmonic has to be excited separately. A solution to these drawbacks can be provided by PRS signals, which are broadband signals having only a few number of signal levels. Therefore, these signals provide fast measurements and are also simple to implement. As a drawback, most PRS signals are only suited for measuring linear systems that makes them unsuited for measuring battery systems, which are nonlinear [16], [21]. However, some PRS signals are capable of reducing the effect of system nonlinearities. From such signals, a three-level ternary sequence signal has been reported to have good performance for battery measurements [15], [24].

In the present article, the ternary-sequence PRS signal is used as perturbation for the battery impedance measurements. The properties of the ternary-sequence are determined by the length of the sequence (N) and the generating frequency (f_{gen}). Together, these parameters define the lowest frequency harmonic of the ternary sequence as

$$f_{\text{min}} = \frac{f_{\text{gen}}}{N}. \tag{26}$$

Fig 6. shows a sample of a 34-b-length ternary sequence in the time domain, and Fig. 7 shows the sequence in the frequency domain. The sequence is generated at 34 Hz. In the time domain, the sequence has only three signal levels making such signal easy to implement to a system. In the frequency-domain, the even-order harmonics have zero energy, which prevents the nonlinear distortion at these harmonics from leaking into the nonzero harmonics. This phenomenon reduces the nonlinear effects of the system in the measurements results [22]. Moreover, there are no sudden changes in the amplitude spectrum of the nonzero harmonics and each harmonic component is equally weighted, making the measurements reliable. However, the amplitudes of the harmonics will decrease to zero at f_{gen}, which limits the highest usable frequency of the measurements as given in (27). [21]

$$f_{\text{max}} = 0.45 f_{\text{gen}}. \tag{27}$$

The design of the ternary-sequence starts by selecting the desired bandwidth of the measurements (f_{min} and f_{max}). For battery impedance measurements, comprehensive characterization of the diffusion region at very low frequencies (<100 mHz) is avoided because this significantly increases the measurement time. Moreover, very low frequencies provide minimal information about the battery state. In addition, inductive behavior at high frequencies (>5 kHz) provide little information about the state of the battery and should not be included in the measurements. In this work, the bandwidth is chosen to cover the charge-transfer region as a whole, as well as, the EoD region, and the beginning of the ohmic/inductive region. For the used LiFePO4 cell, the bandwidth $f_{\text{min}} = 200$ mHz and $f_{\text{max}} = 3.5$ kHz was empirically found to satisfy the foregoing design criteria. The desired f_{gen} can then be obtained by solving it from (27) and further substituting it to (26) to solve N. The

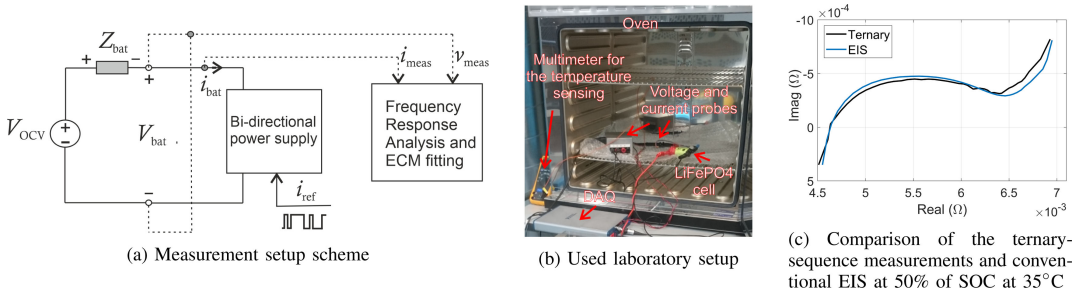

(a) Measurement setup scheme

(b) Used laboratory setup

(c) Comparison of the ternary-sequence measurements and conventional EIS at 50% of SOC at 35°C

Fig. 8. (a) Measurement setup scheme. (b) Used laboratory setup. (c) Comparison of the ternary-sequence measurements and conventional EIS at 50% of SOC at 35 °C.

TABLE I
TERNARY-SEQUENCE DESIGN PARAMETERS FOR THE MEASUREMENTS

Amplitude	f_{gen}	N	f_{min} - f_{max}	MAF windows
1.35A	7.8 kHz	39002	200 mHz - 3.5 kHz	25 and 120

sequence can be generated by applying N to the generation algorithm presented in [22]. However, the generation algorithm accepts limited number of possible values for N in which case the closest possible value to the designed one should be used.

Another important parameter in the perturbation design is the amplitude of the sequence, which is the battery current. The magnitude of the internal impedance of the used LiFePO4 cell is very small (≈ 5 mΩ) that requires high current to introduce a measurable voltage response. The current amplitude should be high enough to produce accurate impedance response from which the zero-derivatives and other required subparameters can be extracted for the proposed fitting algorithm. In turn, the amplitude should be small enough not to disturb the battery nonlinearities nor the application the battery is operating in. To meet these requirements, the amplitude is here chosen according to [24], where LiFePO4 battery of the same capacity, voltage, and internal impedance magnitude was analyzed as in this work. The amplitude design yields to a current of 1.35 A which is relatively small compared to the voltage response magnitude it introduces to the cell in the existing HPPC and EIS studies [3], [6], [18]–[20]. Therefore, the measured impedance spectra is filtered by the moving-average-filter (MAF) in order to guarantee the smoothness of the impedance plot for the ECM fitting [24], [26]. The design of the MAF is carried out according to [24], where two windows (length of 20 and 120) with 25% overlap are applied to the impedance measurements. The ternary-sequence design and MAF parameters from the foregoing derivation for the impedance measurements are shown in Table I.

V. EXPERIMENTS

Fig. 8(a) and (b) illustrates the experiments scheme and the laboratory setup, respectively. In the experiments, the impedance of a LiFePO4 battery cell with a nominal voltage of 3.3 V and a capacity of 2.5 Ah was measured. The ternary sequence was injected to the battery as a current reference for the bidirectional power supply. The offset of the current perturbation is set to zero, which means that the battery is equally charged and discharged during the ternary-sequence measurements. This assures that the SOC is not changing during the measurements that increases the reliability of the measurements. The measurements were carried out in the SOC range 90–10%, with 10% SOC resolution at three different temperatures: 25 °C, 35 °C, and 45 °C. The transition between the SOCs was performed by discharging the cell to the desired SOC with a current of 1 C, where a relaxation time of 1 min was applied to the cell before every measurement. With such short relaxation time, the battery is at the nonequilibrium state and the relaxation time affects to the impedance measurements. Therefore, it is necessary to keep the relaxation time the same to get comparable results. It is suggested in [27] that the relaxation time should be several hours but this is not feasible especially in real-life applications that is why the time is significantly shortened in this article. After the measurements, the resulting impedance was applied by the MAF to smooth the spectra. The measurement data is modified by taking 50 logarithmically distributed data points and neglecting the rest to reduce the amount of data.

The performance of the ternary-sequence measurements is illustrated in Fig. 8(c) in comparison to the conventional EIS measurement applied with similar frequency and amplitude characteristics and configurations than the ternary-sequence measurements. It is shown that the ternary-sequence measurements provide very similar impedance plot than the conventional EIS measurements. Similar results are obtained in [24], where the performance of the ternary-sequence was also validated by the error analysis and by the linear Kronig–Kramers compliance test. The slight differences in the curves can be explained both by the lower signal to noise ration of the ternary-sequence measurements and by the fact that the measurement setups of the ternary-sequence and EIS measurements are slightly different. The EIS is measured with a separate EIS analyzer that cannot be used for the ternary-sequence measurements and vice-versa. Despite the small differences in the curves, the ternary-sequence impedance measurements provide reliable impedance data from which the zero-derivatives and other important parts are clearly obtainable for the further use in the proposed ECM fitting algorithm.

For the fitting process, the absolute value of the difference $||X^{k}_{TSC} - X^{0}_{TSC}||$ in (20) is selected as the convergence limit and the algorithm is stopped when the difference is smaller than 1e−8. The performance of the algorithm is analyzed both in terms of computation time, and normalized-root-mean-square-error (NRMSE). The NRMSE is defined as given in (28), where

TABLE II
DIFFERENT INITIAL CONDITIONS OF THE PARAMETERS AND THE AVERAGE NRMSES OF THE INITIAL FIT ALONG THE SOC AT DIFFERENT TEMPERATURES

	L_s	R_s	R_{CT}	α_{CT}	C_{CT}	α_D	C_D	Average NRMSE (25°C, 35°C, 45°C)
CNLS-init-1	$5e^{-8}$-$5.7e^{-8}$H	$4.7e^{-3}$-$5.1e^{-3}\Omega$	$0.8e^{-3}$-$2.3e^{-3}\Omega$	0.63-0.68	5C-12C	0.46-0.8	540C-910C	$\approx 2.3\%, \approx 4.1\%, \approx 8.8\%$
CNLS-Init-2	$1e^{-8}$H	$5e^{-3}\Omega$	$4e^{-3}\Omega$	0.5	10C	0.65	10000C	$\approx 15\%, \approx 75\%, \approx 150\%$
CNLS-Init-3	1H	1Ω	1Ω	1	1C	1	1C	$\approx 80e6\%, \approx 141e6\%, \approx 200e6\%$

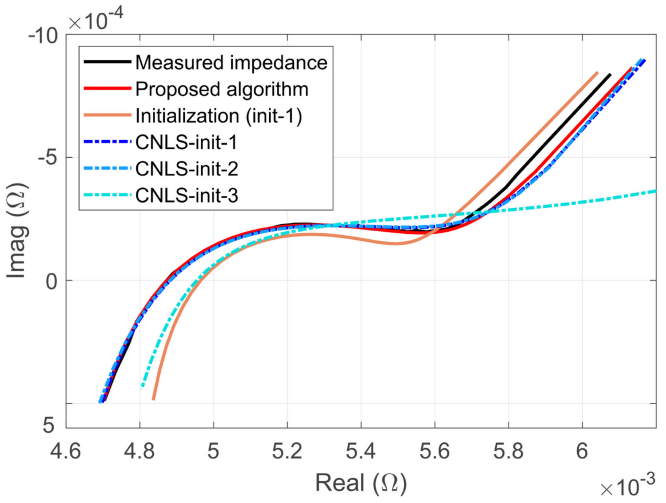

Fig. 9. Impedance plots obtained with different algorithms at 50% of SOC at 45 °C.

Z_{fit} is the fitted impedance, Z_{meas} is the measured impedance, and l is the length of the impedance vectors. For the NRMSE, the maximum absolute difference of the impedance curve is used as the normalization factor.

$$\text{NRMSE} = \frac{\sqrt{\frac{1}{l}\sum_{i=1}^{l}\left(1 - \frac{||Z_{\text{fit}}(i)||}{||Z_{\text{meas}}(i)||}\right)^2}}{\max(||Z_{\text{meas}}||) - \min(||Z_{\text{meas}}||)}. \quad (28)$$

The CNLS fitting is carried out according to [9] by using three different initial conditions that are shown in Table II. The init-1 conditions are obtained adaptively according to the initialization process in Section III-A and the maximum range for the parameters from all SOCs and temperatures are presented in Table II. The init-2 parameters are fixed and obtained empirically according to NRMSE in (28), which is selected to be higher than the init-1 conditions but not drastically inaccurate. For the init-3 conditions, every parameter is fixed to unity that represents the simplest method to obtain the initial conditions that are also highly inaccurate. To discuss the relevance of the selected initial conditions, there is no analytical guideline on what the NRMSE should be for the init-2 and init-3. However, the values in Table II were considered to well establish the cases of accurate with adaptive operation (init-1), relatively accurate guess (init-2) and inaccurate guess (init-3) initial conditions.

VI. RESULTS

The proposed fitting algorithm along with the CNLS with init-1 and -2 provides an accurate match to the measurement data, as illustrated in Fig. 9. Also the proposed initialization produces relatively accurate fit. However, the CNLS-init-3 fails

TABLE III
ECM PARAMETER VALUES FROM FITS IN FIG. 9

	L_s	R_s	R_{CT}	α_{CT}	C_{CT}	α_D	C_D
Proposed alg.	$6.6e^{-8}$H	$4.3e^{-3}\Omega$	$1.4e^{-3}\Omega$	0.48	17.7C	0.68	854C
Init-1	$5.7e^{-8}$H	$4.7e^{-3}\Omega$	$0.8e^{-3}\Omega$	0.64	12.3C	0.65	836C
CNLS-Init-1	$7.0e^{-8}$H	$4.0e^{-3}\Omega$	$1.9e^{-3}\Omega$	0.36	27C	0.72	866C
CNLS-Init-2	$7.2e^{-8}$H	$3.7e^{-3}\Omega$	$2.2e^{-3}\Omega$	0.32	28C	0.74	885C
CNLS-Init-3	$6.1e^{-8}$H	$1.3e^{-7}\Omega$	0.9Ω	0.03	160C	1.0	1200C

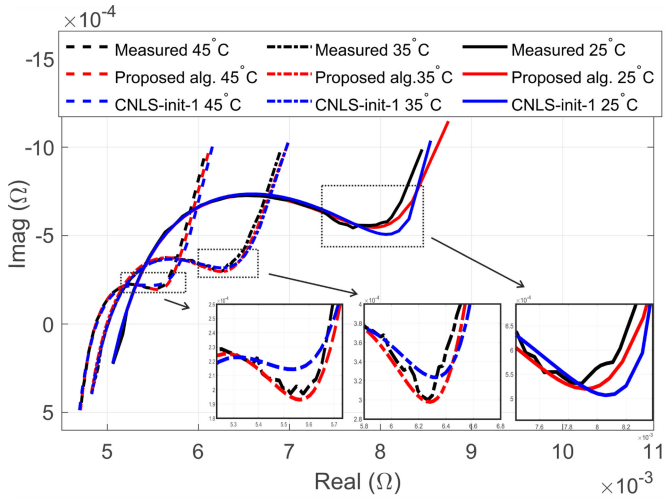

Fig. 10. Impedance plots obtained with the proposed algorithm and CNLS at 50% of SOC at different temperatures.

to fit correctly to the impedance data. Similar results can be concluded from Table III, where the CNLS-init-3 parameters greatly differ from the parameters provided by other fittings. This is most likely caused by the fact that the CNLS-init-3 found different local minimum than the other CNLSs due to the poor selection of the initial conditions [9]. The larger NRMSE values in Table IV also indicate the weak performance although they are remained relatively low. This is due to the fact that the fit is located close to the measured curve even though it cannot adapt to its shape.

The lowest fitting error is achieved by the CNLS when the initial conditions are appropriately chosen (init-1 and -2). Despite the slightly larger error of the proposed algorithm, it fits the EoD and the diffusion region more accurately than the CNLS as shown in Fig. 10. Thus, the proposed algorithm has more consistent performance throughout the impedance curve than the CNLS that provides very accurate fit in the charge transfer and ohmic/inductive regions. Compared to these regions, the diffusion region has fewer data points that have smaller effect on the NRMSE values. By taking the quantitative and graphical analysis into account, it can be stated that the performances of the proposed algorithm and CNLS init-1 and -2 are very similar in terms of the fitting accuracy.

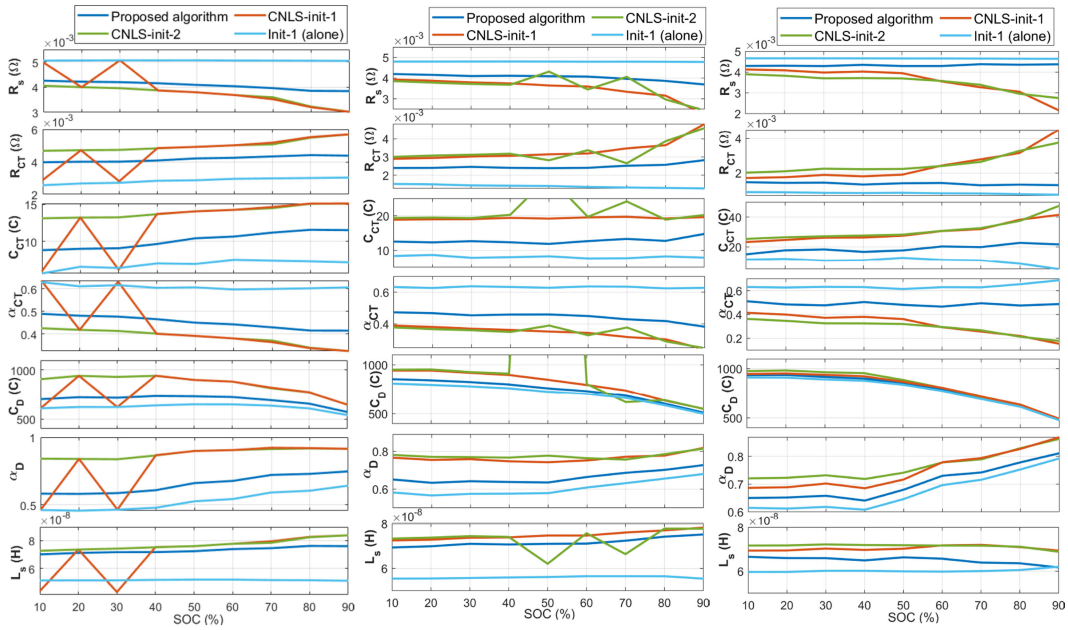

(a) $25°C$ (b) $35°C$ (c) $45°C$

Fig. 11. Fitted ECM parameters as a function of SOC at various temperatures. (a) 25 °C. (b) 35 °C. (c) 45 °C.

The proposed algorithm is 7–10 times faster than the fastest CNLS at all temperatures. This is because the proposed algorithm has no complex calculations included while the CNLS utilizes matrix products that require more computation time [9]. The initial conditions have also significant effect on the fitting time of CNLSs. Especially, the CNLS-init-3 has 2–3 times longer fitting time. The proposed initialization also slightly makes the fitting faster compared to init-2 fitting time. Although the NRMSE values of init-1 and -2 are generally similar, the proposed initialization provides adaptively obtained initial conditions, which ensures the robustness of the CNLS at different temperatures. This is expected to be even more beneficial at more extreme temperatures where the impedance and, thus, the ECM parameter values are changing even more.

The parameter values from the fitting algorithms are shown as a function of SOC at different temperatures in Fig. 11. The parameters from CNLS-init-3 are omitted due to its weak performance. The proposed algorithm is shown to have more consistent trends in the parameters at all temperatures than CNLSs. The adaptive performance of the proposed initialization can also be concluded from Fig. 11. The CNLS-init-1 parameters have mismatch at 25°C and CNLS-init-2 at 35 °C, which can also be seen from the increased NRMSE at the corresponding SOCs in Table IV. The fitting error of the CNLS at these specific SOCs could most likely be fixed by tightening the convergence and boundary conditions of the algorithm [10]. However, this would make the fitting process to last even longer. Moreover, the parameter values of the proposed algorithm and the CNLS are very different although the NRMSE difference of the algorithms is relatively small. This also applies to the parameter values of the CNLS init-2 and -3 that have similar NRMSE but a little different parameter values as shown in Fig. 11 and Table III.

TABLE IV
FITTING ERRORS AT VARIOUS SOCS AND TEMPERATURES

SOC	90%	70%	50%	30%	10%	
Measurements at $25°C$						
Algorithm	**NRMSE**					**average fit time**
init-1	3.7%	2.5%	2.3%	2.8%	2.6%	1.5ms
Prop.-algorithm	1.2%	1.3%	1.3%	1.3%	1.3%	7ms
CNLS-init-1	1.0%	0.7%	0.7%	2.9%	1.7%	65ms
CNLS-init-2	1.0%	0.7%	0.7%	0.6%	0.7%	67ms
CNLS-init-3	4.8%	4.9%	4.8%	2.2%	4.7%	207ms
Measurements at $35°C$						
Algorithm	**NRMSE**					**average fit time**
init-1	5.6%	5.0%	3.9%	2.8%	2.9%	1.5ms
Prop. algorithm	1.8%	1.7%	1.5%	1.3%	1.3%	9ms
CNLS-init-1	1.3%	1.3%	1.1%	1.0%	1.0%	65ms
CNLS-init-2	1.4%	2.1%	5.5%	0.9%	1.0%	69ms
CNLS-init-3	2.5%	5.1%	4.2%	4.2%	4.4%	143ms
Measurements at $45°C$						
Algorithm	**NRMSE**					**average fit time**
init-1	8.8%	7.1%	5.2%	4.0%	3.9%	1.5ms
Prop. algorithm	4.2%	3.8%	2.6%	2.0%	1.8%	9ms
CNLS-init-1	3.0%	2.3%	1.8%	1.6%	1.6%	90ms
CNLS-init-2	3.0%	2.3%	1.8%	1.6%	1.6%	100ms
CNLS-init-3	15%	10%	5.7%	3.4%	5.6%	182ms

This clearly states that there are more than one possible combinations for the parameters to fit to the measurement data and the performance cannot be compared based on the magnitude of the parameters. This can be explained by the fact that the minimization problem of the proposed algorithm is very different to that of the CNLS [9], [10]. Therefore, adaptively obtained initial conditions can provide consistent starting values for the CNLS. This can guarantee more robust performance in changing operating conditions than the randomly obtained fixed initial conditions. However, in terms of fitting accuracy, time, and the consistency of the parameters, the performance of the proposed

fitting algorithm can be considered to be even better than the CNLS with any initial conditions.

The diffusion region parameters (C_{D} and α_{D}) seem to have most characteristic trends at all temperatures. This is in line with the recognized fact that the battery impedance has strongest SOC-dependency at the diffusion region [5]. Other ECM parameters have less distinguishing trends at all temperatures, which is also shown in previous studies [4], [5], [14]. This is considered to be caused by the nonlinearity of the ECM that effect is significant especially at the charge-transfer and ohmic regions. However, the proposed algorithm is able to keep some of the parameters in these regions more constant than the CNLS. This is especially true for the resistance R_{s}, which should be remained relatively constant as a function of SOC for LiFePO4 batteries [5], [14]. Furthermore, the battery nonequilibrium state may have effect on the inconsistencies of the parameters, since the used relaxation time before measurements is only 1 min. This is significantly lower than what is generally suggested to allow the battery reach equilibrium [27]. Therefore, the effect of such short relaxation time should be considered when utilizing the impedance for state-estimation algorithms. Despite the inconsistency of the parameters, the extracted ECM parameters provide an accurate fit to the measurement data, which is valuable for the dynamic analysis and simulations of the battery.

VII. Conclusion

This article proposed a novel fitting algorithm for extracting the battery ECM parameters from the measured impedance data. The performance of the algorithm was validated for real LiFePO4-cell impedance data measured with a ternary sequence PRS signal at various SOCs and temperatures. The performance of the algorithm was also compared to the conventional CNLS algorithm with different initial conditions. It showed that the proposed algorithm was computationally light and provides accurate fit to the impedance data. The performance of the proposed algorithm was also more consistent at all regions of the impedance curves at all SOCs and temperatures. The initialization process of the proposed algorithm was discovered as an effective tool to adaptively obtain the initial conditions also for the CNLS. Moreover, some of the ECM parameters were observed to have consistent dependency to the battery SOC at various temperatures. The results also showed that together with the ternary sequence measurements, the proposed algorithm has the potential to be utilized for battery dynamics analysis, as well as for the battery state estimation in practical battery applications.

References

[1] J. Meng *et al.*, "An overview and comparison of online implementable SOC estimation methods for lithium-ion battery," *IEEE Trans. Ind. Appl.*, vol. 54, no. 2, pp. 1583–1591, Mar. 2018.

[2] M. Berecibar, I. Gandiaga, I. Villarreal, N. Omar, J. Van Mierlo, and P. Van den Bossche, "Critical review of state of health estimation methods of Li-ion batteries for real applications," *Renew. Sustain. Energy Rev.*, vol. 56, pp. 572–587, Apr. 2016.

[3] R. Xiong, J. Tian, W. Shen, and F. Sun, "A novel fractional order model for state of charge estimation in lithium ion batteries," *IEEE Trans. Veh. Technol.*, vol. 68, no. 5, pp. 4130–4139, May 2019.

[4] X. Wang, X. Wei, and H. Dai, "Estimation of state of health of lithium-ion batteries based on charge transfer resistance considering different temperature and state of charge," *J. Energy Storage*, vol. 21, pp. 618–631, 2019.

[5] D. I. Stroe, M. Swierczynski, A. I. Stan, V. Knap, R. Teodorescu, and S. J. Andreasen, "Diagnosis of lithium-ion batteries state-of-health based on electrochemical impedance spectroscopy technique," in *Proc. IEEE Energy Convers. Congr. Expo.*, Sep. 2014, pp. 4576–4582.

[6] J. Tian, R. Xiong, and Q. Yu, "Fractional-order model-based incremental capacity analysis for degradation state recognition of lithium-ion batteries," *IEEE Trans. Ind. Electron.*, vol. 66, no. 2, pp. 1576–1584, Feb. 2019.

[7] Y. Zou, S. E. Li, B. Shao, and B. Wang, "State-space model with non-integer order derivatives for lithium-ion battery," *Appl. Energy*, vol. 161, pp. 330–336, 2016.

[8] C. Zou, X. Hu, S. Dey, L. Zhang, and X. Tang, "Nonlinear fractional-order estimator with guaranteed robustness and stability for lithium-ion batteries," *IEEE Trans. Ind. Electron.*, vol. 65, no. 7, pp. 5951–5961, Jul. 2018.

[9] D. M. Bates and D. G. Watts, Eds., *Nonlinear Regression Analysis and Its Applications* (Wiley Series in Probability and Statistics). Hoboken, NJ, USA: Wiley, Aug. 1988.

[10] M. Žic, "Solving CNLS problems by using Levenberg-Marquardt algorithm: A new approach to avoid off-limits values during a fit," *J. Electroanalytical Chem.*, vol. 799, pp. 242–248, Aug. 2017.

[11] S. M. M. Alavi, C. R. Birkl, and D. A. Howey, "Time-domain fitting of battery electrochemical impedance models," *J. Power Sour.*, vol. 288, pp. 345–352, 2015.

[12] S. R. Nelatury and P. Singh, "Extracting equivalent circuit parameters of lead–acid cells from sparse impedance measurements," *J. Power Sour.*, vol. 112, no. 2, pp. 621–625, Nov. 2002.

[13] S. M. R. Islam and S.-Y. Park, "Circuit parameters extraction algorithm for a lithium-ion battery charging system incorporated with electrochemical impedance spectroscopy," in *Proc. IEEE Appl. Power Electron. Conf. Expo.*, 2018, pp. 3353–3358.

[14] P. Vyroubal and T. Kazda, "Equivalent circuit model parameters extraction for lithium ion batteries using electrochemical impedance spectroscopy," *J. Energy Storage*, vol. 15, pp. 23–31, Feb. 2018.

[15] J. Sihvo, T. Roinila, T. Messo, and D.-I. Stroe, "Novel online fitting algorithm for impedance-based state estimation of Li-ion batteries," in *Proc. IEEE Ind. Electron. Conf.*, 2019, pp. 4531–4536.

[16] A. Lasia, *Electrochemical Impedance Spectroscopy and its Applications*. New York, NY, USA: Springer, 2014.

[17] E. Karden, S. Buller, and R. W. De Doncker, "A method for measurement and interpretation of impedance spectra for industrial batteries," *J. Power Sour.*, vol. 85, no. 1, pp. 72–78, 2000.

[18] J. J. Giner-Sanz, E. M. Ortega, and V. Pérez-Herranz, "Optimization of the perturbation amplitude for EIS measurements using a total harmonic distortion based method," *J. Electrochem. Soc.*, vol. 165, no. 10, pp. E488–E497, Jul. 2018.

[19] E. Din, C. Schaef, K. Moffat, and J. T. Stauth, "A scalable active battery management system with embedded real-time electrochemical impedance spectroscopy," *IEEE Trans. Power Electron.*, vol. 32, no. 7, pp. 5688–5698, Jul. 2017.

[20] W. Huang and J. A. Qahouq, "An online battery impedance measurement method using DC-DC power converter control," *IEEE Trans. Ind. Electron.*, vol. 61, no. 11, pp. 5987–5995, Nov. 2014.

[21] K. Godfrey, *Perturbation Signals for System Identification*. Englewood Cliffs, NJ, USA: Prentice Hall, 1993.

[22] A. H. Tan and K. R. Godfrey, "The generation of binary and near-binary pseudorandom signals: An overview," *IEEE Trans. Instrum. Meas.*, vol. 51, no. 4, pp. 583–588, Aug. 2002.

[23] T. Roinila *et al.*, "Hardware-in-the-loop methods for real-time frequency-response measurements of onboard power distribution systems," *IEEE Trans. Ind. Electron.*, vol. 66, no. 7, pp. 5769–5777, Jul. 2019.

[24] J. Sihvo, D. Stroe, T. Messo, and T. Roinila, "Fast approach for battery impedance identification using pseudo-random sequence signals," *IEEE Trans. Power Electron.*, vol. 35, no. 3, pp. 2548–2557, Mar. 2020.

[25] J. Vetter, P. Nov, M. R. Wagner, and C. Veit, "Ageing mechanisms in lithium-ion batteries," *J. Power Sour.*, vol. 147, pp. 269–281, 2005.

[26] P. Manganiello, G. Petrone, M. Giannattasio, E. Monmasson, and G. Spagnuolo, "FPGA implementation of the EIS technique for the on-line diagnosis of fuel-cell systems," in *Proc. IEEE 26th Int. Symp. Ind. Electron.*, Jun. 2017, pp. 981–986.

[27] A. Barai, G. H. Chouchelamane, Y. Guo, A. McGordon, and P. Jennings, "A study on the impact of lithium-ion cell relaxation on electrochemical impedance spectroscopy," *J. Power Sour.*, vol. 280, pp. 74–80, 2015.

Jussi Sihvo (Student Member, IEEE) received the M.Sc. degree in electrical engineering from the Tampere University of Technology, Tampere, Finland, in 2018. He is currently working on Diagnostics and analysis of Li-ion batteries and grid-connected enegy storages with the Faculty of Information Technology and Communication Sciences, Tampere University.

He was also a Visiting Researcher with Aalborg University, Denmark, in 2018. His research interests include modeling, diagnostics, and analysis of Li-ion batteries and grid-connected converters.

Tomi Roinila (Member, IEEE) received the M.Sc. (Tech.) and Dr.Tech. degrees in automation and control engineering from the Tampere University of Technology, Tampere, Finland, in 2006 and 2010, respectively.

He is currently an Assistant Professor with Tampere University. His main research interests include modeling and control of grid-connected power-electronics systems, and analysis and modeling of energy storage systems.

Daniel-Ioan Stroe (Member, IEEE) received the Dipl.-Ing. degree in automatics from "Transilvania" University of Brasov, Romania, in 2008, the M.Sc. degree in wind power systems from Aalborg University, Aalborg, Denmark, in 2010, and the Ph.D. degree in lifetime modeling of lithium-ion batteries from Aalborg University, in 2014.

He has been with Aalborg University, since 2010. Currently, he is an Associate Professor with the Department of Energy Technology, where he leads the Battery Storage Systems Research Programme and the Battery Systems Testing Lab. He was a Visiting Researcher with RWTH Aachen, Germany, in 2013. He has coauthored more than 100 journal and conference papers in various battery-related topics. His current research interests include energy storage systems for grid and e-mobility, lithium-based batteries testing, modeling, diagnostics and their lifetime estimation.